Characterisation of Shear Turbulence in a Wide Gap and Large Size Taylor-Couette Flow Reactor

Chenyang Xue[a], Xiaogang Yang[a,*], Guang Li[a], Bingjian Liu[a], Jie Yang[b]

[a]Department of Mechanical, Materials and Manufacturing Engineering
University of Nottingham Ningbo China
Ningbo 315100, PR China

[b]Department of Physics & Mathematics
University of Hull
Hull HU6 7RX, UK

Abstract

The instability of the supercritical Taylor-Couette flows has been extensively investigated in many previous studies but only few studies focusing on shear turbulence characteristics in wide gap and large size Taylor-Couette flow (TCF) reactors have been conducted. In the present study, particle image velocimetry (PIV) technology was adopted to investigate such shear turbulence characteristics based on the measurement of the instantaneous axial and radial velocities in the meridional plane of the annulus between the rotating inner and the non-rotating outer cylinder in a large size TCF reactor. The experimental results have indicated that as the Reynolds number $Re_T = \frac{r_i \omega d_{gap}}{\nu}$increases, exceeding the critical value of 7300, the vorticity strength of the induced Taylor vortices remarkably increases, consequently causing a much enhanced outward impinging jet flow between the pair of Taylor vortices. It was also found that the occurrence of the secondary vortices in addition to the major Taylor vortices when Re_T reaches a critical value, significantly alternating the flow and turbulent characteristics in the reactor. It was also demonstrated that the gravitational force because of the vertical placement of the TCF reactor affects the flow both in radial and parallel (axial) direction but such effect in its parallel direction is much stronger than that in radial direction. Turbulent energy dissipation rate distribution and turbulent kinetic energy (TKE) spectra were also obtained using 2D PIV measured turbulent velocity fluctuation gradients.

***Keywords*:** Taylor-Couette flow reactor; shear turbulence; PIV measurement; intensification

*Corresponding author:

Tel: +86-574-88180000 Ext 8419 E-mail: Xiaogang.Yang@nottingham.edu.cn (X.Yang)

1. Introduction

In a wide range of industrial application, the production of find powder particles is very important, such as bio-chemical and pharmaceutical productions. Because particle size and morphology significantly affect the synthesized particle properties (Randolph and Larson, 1988), the use of shear turbulence controllable synthesis of particles can be realised by using specially designed reactors such as TCF reactor. It has now been widely noticed that certain pattern of toroidal vortex can be formed after the system reaches a critical condition, i.e Taylor vortex flow (TVF). This critical condition can be judged by the Reynolds number (Re) based on the gap width, $Re_T = \frac{r_i \omega d_{gap}}{\nu}$. In the case of large Re, a phenomenon of a secondary instability can be found, which causes the flow to become time-dependent and deformation of the vortices, referred to as wavy vortex flow (WVF). With further increasing the Re number, the wavy flow may transit to turbulent state and even develop into highly turbulent. However, for a wide gap TCF reactor which has a large inner cylinder size, the turbulent shear turbulence characteristics and instability has not been fully explored.

Andereck *et al*. (1986), using aluminium flakes, reports a comprehensive characterisation of different fluid dynamic cases in a Taylor-Couette where inner cylinder and outer cycliner were both free to rotate and successfully showed coherent structures. Reynolds number defined by $Re = R_i \omega d_{gap}/\nu$ was used to describe the dynamic conditions. They have demonstrated that at different Re, flow pattern varies to correspond to different regimes from TVF (Taylor 1923), WVF (Coles 1965), modulated WVF (Gorman and Swinney 1979), and turbulent Taylor vortex flow (TTVF) (Smith and Townsend 1982) to fully turbulent flow (FTF) (Smith and Townsend 1982). These flow pattern changes will certainly affect the process of producing and synthesis powder particles when adopting the TC as the reactor because the particles will have a strong interaction with the turbulent eddies embedded in these Taylor vortices especially when the flow has been developed into the fully turbulent regime.

In order to fully reveal the features of the flow in TCFs, particle image velocimetry technique has been adopted into the investigation of Taylor Couette reactor since Wereley and Lueptow (1998, 1999) firstly performed a 2D PIV measurement on the velocity distribution in the radial-axial cutting plane in a Taylor Couette reactor. Since then, 2D PIV has been widely used to examine different flow characteristics of Taylor–Couette flows. In the work of Akonur and Lueptow (2003), an investigation on the flow velocities of Taylor Couette reactor in radial-

circumferential cross-section plane was performed. The results are compared with those obtained by Wereley and Lueptow (1998, 1999) and velocity components of all three directions were thus be obtained. The work conducted by these authors, however, has been focused on the use of the PIV measurement to analyse the volumetric flow structures in a Taylor–Couette system. Ravelet et al. (2010) has recently applied the Stereo PIV to measure the Taylor–Couette flow, again performing the measurements on the axial–radial cutting plane of the flow field. A more comprehensive summary of the experimental studies on TCFs is listed in Table 1, which shows all the measurements for TCFs made by previous studies using the PIV techniques and the experimental conditions. In most of these studies, only small size of TCF apparatus or reactors was adopted. It should be noted that Huisman *et al* (2011) used this technique to measure the flow in a relatively large size Taylor-Couette setup with an inner cylinder of 200mm in diameter but only focusing on the flow characteristics in r-θ plane so that the characteristics of the actual torque applied to the reactor based on turbulent energy dissipation rate measured could be evaluated. A more comprehensive study (Racina *et al*., 2006) has focused on the adoption of PIV technique to measure and obtain the turbulent dissipation rate and local micro-mixing time using a relatively small TC reactor with an inner diameter of 100 mm of outer cylinder. The use of a 3D tomographic investigation on the TC flow with a Reynolds number Re reaching 23500 has been also reported by Tokgoz *et al* (2012). However, due to the measurement accuracy limitation of 3D PIV technique, the estimation of the turbulence dissipation rates obtained based on the 3D flow field did not show an agreement with the well-known Kolmogorov -5/3 power scaling law.

In sum, almost the previous studies on flow characteristics in TCF reactors are confined to the flow regimes that are limited into TVF, WVF, MWVF and CWVF. Quite a few studies reveal the flow characters of high Reynolds number falling in the TTVF and FTF flow pattern through PIV technique. The studies of TTVF and FTF are mainly focused on torque and power-law scaling from current literatures. Wendt (1933) reported the results of Re from 50 to 10^5 with only orque measurements in the TC reactor. Following the same path, results from Tong *et al*. (1990) also showed power-law scaling G~Re over the range of 4e4 to 4e5 and fit the empirical power-law well. Although power-law shows averaged or overall flow characters, such as averaged dissipation rate, averaged micro-mixing time or averaged Kolmogorov scale, few local flow properties and distributions can be revealed.

In the present study, the use of a 2D PIV to measure the TCFs in a wide gap and large size TCF reactor will be conducted. The TC reactor which has a large outer-cylinder with the diameter of 300 mm and length of 600 mm. The PIV measurement was carried out in a wide range of Reynolds numbers varying from 1800 to 21600 to cover the transit turbulent vortex flow (TTVF) and fully turbulent flow (FTF) patterns. This paper is organized in such a way. Section 2 introduces the experimental setup and flow visualization methods while section 3 will present such as turbulent shear flow velocity field and velocity distribution, vorticity distribution and turbulent energy dissipation rate and discussion on shear turbulence characteristics. Section 4 will give out the conclusions reached from the present study.

2. Experimental Setup and Validation

The PIV measurements were performed using a laboratory scale TCF reactor with inner and outer cylinders' radii are R_i = 120 mm and R_o = 150 mm, respectively, and therefore the gpa ratio is $g = R_i / R_o = 0.8$. The gap size $d_{gap} = R_o - R_i = 30$ mm, and the length of the inner cylinder is H = 300 mm, therefore, the axial aspect ratio is $\Gamma = H/d = 10$. The experimental setup is shown in Figure 1. The system is closed by the top and bottom lids, which are fixed to the outer cylinder while the outer cylinder is fixed to a support frame. The outer cylinder of the TC reactor is transparent, allowing the optical access and visualisation. The surface of inner cylinder was coated with an immiscible black paint to avoid optical reflection and reduce the optical background noise. It has been found that this measure has considerably improved the quality of the images. The PIV field of view window covers the range of (1/5~2/5)H measured from the bottom of the TC reactor.

The system (from Dantec) is consisted of the laser Nd:YAG (532nm of wave length , 2×30 MJ of laser energy), a high resolution CCD camera (2048 × 2048 pixels^2, 5Hz), a Nikon lens (AF 50mm F/1.8D), a timer box (Dantec Dynamics). A dual laser sheets were used to illuminate the $r - \theta$ plane of TCF reactor synchronized with the CCD camera which set to be 5Hz. In image processing, 16 × 16 pixel^2 (with 50% overlap) of cell area (0.472×0.472mm) were used to capture the velocity vector field. The measurements were taken and the images were captured after the TC reactor was initiated to run for 10 minutes (at least 100 revolutions), which ensures the Taylor vortices or turbulent flow to be fully established. In order to minimize the end effect of the cylinders of the Taylor–Couette facility on the measurement results, the

images were recorded near the mid-height of the cutting plane of the TC reactor as shown in Figure 2.

3. Results and Discussion

3.1 Time averaged velocity field

In Figure 3a and Figure 3b time averaged streamline and velocity field are plotted. In these figures, the magnitude of local velocity are normalized using $\Omega \times R_i$, in different Reynolds numbers. The colour of the vectors shows that the relative velocity for the case of low Reynolds number, especially in the radial direction, is higher than that for high Reynolds number conditions. This indicates that the convective transport efficiency relatively drops as Re increases. The Taylor vortices patterns change with the Reynolds number. The aspect ratio (length in axial direction over length in radial direction) of each cell of the Taylor vortices decreases as Reynolds number increases (roughly from 1.40 to 1.25 and then stabilized in 1.00).

From Figure 3, it reveals that Taylor vortices clearly repeat their patterns but the cell width of the vortices has been extended with increase of the Reynolds number. The amplitude of dimensionless radial velocity decreases with the Reynolds number, which indicates that the centrifugal force has a remarkable influence on Taylor vortices in low Re case than in High Re case. The maximum and minimum radial and axial velocities at different Re is shown in Figure 4. Such velocity difference between the maximum and minimum for radial and axial velocities may be able to represent the variation of Taylor vortex pair cell width at different Re. In addition, the phase shifted in different Re condition means the Taylor vortex length difference and end wall effect have a different influence at different Re. However, for all four Re conditions, the amplitude of dimensionless radial velocity of one location in the Taylor vortex is slightly larger than that of the same location for a lower Taylor vortex pair. This may be attributed to the impact of the gravity of the hydrostatic pressure on the radial velocity.

From Figure 4, it also shows that the maximum and minimum time-averaged velocities based on the line average on the vertical centreline linearly change with the Reynolds number. For the axial velocity, the difference between the minimum and maximum velocity component is much smaller than that for radial velocity component. This is very apparent for the minimum axial velocity. This indicate that the gravity has a significant influence on the Taylor vortex averaged velocity field. And this agrees with the results from Figure 3, the reverse flow at large

Re is not vertical to the walls, which is the results of the increasing axial velocity and radial velocity if not synchronized.

3.2 Vortex and coherent structure distribution

In order to clearly show the vortex pattern variation with the Reynolds number, the average vorticity distribution is shown in Figure 4 for the given Reynolds number varying from 7300 to 21600. The vorticity is estimated by

$$\Omega = \nabla \times \boldsymbol{u} \tag{1}$$

As only velocity components in radius and axil direction are available from the PIV measurement, the vorticity observed in the r-z plane can be estimated according to:

$$\omega_\theta = \frac{\partial u_r}{\partial z} - \frac{\partial u_z}{\partial r} \tag{2}$$

In Figure 5, the pairing Taylor counter-flowing vortices can be easily identified and the aspect ratio to characterise the Taylor vortices increases as Reynolds number increases. The secondary vortices can be observed in the vicinity of the outer cylinder boundary. Following the same pattern as the velocity fields, the region of secondary vortices shrinks as Reynolds number increases. This may be attributed the enhanced outward impinging jet flow. The stagnation zones were observed to occur on the locations where the impinging jet impacts on the outer wall and the counter-flowing from the vortex pair, accompanying by the appearance of strong vorticity. It should be noted that the impact of the impinging jet flow on the wall causes the occurrence of secondary vortices that are couched between two major Taylor vortices.

The time averaged *Q*-criteria proposed by Hunt *et al*. (1988) and shear strain in radius and axial plane are plotted at different Reynolds number are displayed in Figures 6 and 7, respectively. It can be seen from the figures that the coherent structures illustrated by *Q*, defined by equation (3), clearly indicates the existence of apparent vortex coherent structures of Taylor vortices. At low Reynolds number, the high Q value mainly takes place and concentrates in the cores of Taylor vortices. The secondary vortex coherent structure can also be observed based on the *Q* value near the walls. With increasing in the Reynolds number, the coherent structure region tends to be diffusive, indicating the features of fully turbulence. The boundary used to characterise the Taylor vortices starts to become blur and the secondary vortices near the inner or outer cylinders seems to disappear. Also, when Reynolds number increases, the vortex coherent structures have been visualised to be twisted and spread and the vortices are connected

each other. This observation can also be consolidated by showing the streamlines in Figure 8 and the vortex core locations displayed in Figure 9.

$$Q = \frac{\partial u_r}{\partial r}\frac{\partial u_z}{\partial z} - \frac{\partial u_r}{\partial z}\frac{\partial u_z}{\partial r} \tag{3}$$

Similarly, the spatial distribution of shear strain in the r-z plane also changes as Re increases. From Figure 7 (Both red and blue colours show the occurrence of high turbulent shear stresses as the Taylor vortices are counter-flowing but green colour shows the lower turbulent shear stress zone), higher turbulent shear stresses are observed to take place in the zones of near wall, outward and inward impinge jet flow and counter-flows. Lower turbulent shear stresses occur in the core of Taylor vortices. Further inspection reveals that the magnitudes of turbulent shear stresses in the counter-flow zone are smaller than those in the impinging jet flow zone. This can be explained by the fact that with increasing in the Reynolds number, the momentum transported by the stronger shear turbulence in the outward impinging jet flow is remarkably strengthened, resulting in a stronger local turbulent shear stress distribution. Apart from this, the area of high turbulent shear stress region also expands, consistent with the observation that the Taylor vortex cell becomes wider as the outward impinging jet from inner to outer cylinder between TCF vortex cells to push the vortices apart with the climb of the Re.

The spatial distortion of TCF vortices with the growing of the Re can be revealed easily by inspecting the instantaneous velocity field as shown in Figure 8 where the time sequence evolution of the instantaneous velocity field variations (time interval: 0.2 s) is presented with the red dot labels the core positions of vortex coherent structures. In the case of Re=7300, the completed Taylor vortices pair can be identified in the instantaneous velocity field. Due to the impact of hydrostatic pressure due to the gravity, the upper vortex in the Taylor vortices is stretched slightly longer than the lower vortex in the Taylor vortex pair. The shape of the vortices is basically time independent while the impinging jet flow region varies noticeably with the time. The impinging jet flow is twisted and a wavy pattern can be recognized. The cores of the Taylor vortices have shifted slightly and minor distortion can be found in some areas of the instantaneous velocity field. It is noticed that when Re = 11500, the complete Taylor vortex pair can still be identified and the gravity effect seems to be still weak. Consequently, the vortex structure is twisted but not stretched. Further increase of the Re results in the vortices being twisted as the outward impinging jet flow brings out the vortices

to separate each other and causes the wavy fluctuation of Taylor vortices with time, as can be affirmed by looking into the case of Re=21300. From Figure 8 it shows that the cores in the Taylor vortices start to migrate accompanied by a severe distortion of the shape of Taylor vortices and the Taylor vortices start to wobble and become unstable. It should be noted here that though a clear outward impinging jet flow and pair counter-flow regions can be still identified with separation between each Taylor vortex, the distortion has resulted in a difficult visualisation of Taylor vortices. Moreover, the outward impinging jet flow's wavy pattern becomes stronger and induces turbulent eddies in smaller scales.

The above mentioned turbulent Taylor vortex evolution and distortion with the Reynolds number can be demonstrated by displaying the vortex core locations as shown in Figure 9, where Taylor vortex core locations based on assembling the collections over 200 time intervals based on the time averaged vortex core shown in Figure 3 are presented. In the figure, it reveals that the locations of the cores change with the time. As the Reynolds number increases, the area where the vortex core appears starts to expand and smears into the regions nearing the wall and counter-flow region. It should be noted particularly that unlike high turbulent shear stress region, the coherent structures are less likely to appear in the impinging jet flow region than those in the counter-flow region. This implies that a highly turbulent fluctuations in the flow may not always give out a vortex coherent structure. Small or micro particles are more likely to be trapped in the counter-flow region in the Taylor Couette flow reactor, where a relatively lower shear strain than the outward impinging jet flow region can be found.

3.3 Characteristics of shear turbulence energy dissipation rate

As the flow in the TCF reactor has been developed into a fully developed turbulent flow, it would be very interested in showing the distribution of turbulence energy dissipation rate in the reactor. Dissipation rate is still described and defined by

$$\varepsilon = 2\overline{\nu s'_{ij} s'_{ij}} = \frac{1}{2}\nu \overline{\left(\frac{\partial u'_i}{\partial x_j} + \frac{\partial u'_j}{\partial x_i}\right)^2} \tag{4}$$

The corresponding turbulent shear rates will be evaluated based on the PIV experimental measurement results. Typical instantaneous velocity components, u_r and u_z, plotted against a

time period of 200 s at the location of $r = \frac{d_{gap}}{2}, z = \frac{H}{2}$ is shown in Figure 10. In the cylindrical coordinate system, equation (3-4) can be written as

$$\varepsilon = \nu\left\{2\overline{\left(\frac{\partial u_r'}{\partial r}\right)^2} + 2\overline{\left(\frac{\partial u_z'}{\partial z}\right)^2} + 2\overline{\left(\frac{\partial u_\theta'}{r\partial\theta}\right)^2} + \overline{\left(\frac{\partial u_r'}{\partial z}\right)^2} + \overline{\left(\frac{\partial u_z'}{\partial r}\right)^2} + \overline{\left(\frac{\partial u_r'}{r\partial\theta}\right)^2} + \overline{\left(\frac{\partial u_\theta'}{\partial r}\right)^2} + \overline{\left(\frac{\partial u_z'}{r\partial\theta}\right)^2} + \overline{\left(\frac{\partial u_\theta'}{\partial z}\right)^2} + 2\overline{\left(\frac{\partial u_r'}{\partial z}\frac{\partial u_z'}{\partial r}\right)} + 2\overline{\left(\frac{\partial u_r'}{r\partial\theta}\frac{\partial u_\theta'}{\partial r}\right)} + 2\overline{\left(\frac{\partial u_z'}{r\partial\theta}\frac{\partial u_\theta'}{\partial z}\right)}\right\} \quad (5)$$

As velocity components can only be measured by using the 2D PIV in the r-z plane, the third component in θ direction has to be estimated based on the two others using the method and assumptions proposed by Sharp *et al*. (2000). The use of the known or measured components for estimation of the unknown component in the third direction based on the assumption that the turbulence characteristics of the turbulent flow is statistically isotropic, at least being locally isotropic, is now widely recognised. The currently investigated turbulent flow in the TCF reactor can be assumed to satisfy such condition. Thus, the average of two known terms can yield the estimation of the unknown term in θ direction, which read

$$\overline{\left(\frac{\partial u_\theta'}{r\partial\theta}\right)^2} = \frac{1}{2}\left(\overline{\left(\frac{\partial u_r'}{\partial r}\right)^2} + \overline{\left(\frac{\partial u_z'}{\partial z}\right)^2}\right) \quad (5a)$$

$$\overline{\left(\frac{\partial u_r'}{r\partial\theta}\right)^2} = \overline{\left(\frac{\partial u_\theta'}{\partial r}\right)^2} = \overline{\left(\frac{\partial u_z'}{r\partial\theta}\right)^2} = \overline{\left(\frac{\partial u_\theta'}{\partial z}\right)^2} = \frac{1}{2}\left(\overline{\left(\frac{\partial u_r'}{\partial z}\right)^2} + \overline{\left(\frac{\partial u_z'}{\partial r}\right)^2}\right) \quad (5b)$$

$$\overline{\left(\frac{\partial u_r'}{r\partial\theta}\frac{\partial u_\theta'}{\partial r}\right)} = \overline{\left(\frac{\partial u_z'}{r\partial\theta}\frac{\partial u_\theta'}{\partial z}\right)} = -\frac{1}{4}\left(\overline{\left(\frac{\partial u_r'}{\partial r}\right)^2} + \overline{\left(\frac{\partial u_z'}{\partial z}\right)^2}\right) \quad (5c)$$

This leads to the following estimation for the local time averaged turbulent energy dissipation rate estimated from the 2D PIV data:

$$\varepsilon = \nu\left\{2\overline{\left(\frac{\partial u_r'}{\partial r}\right)^2} + 2\overline{\left(\frac{\partial u_z'}{\partial z}\right)^2} + 3\overline{\left(\frac{\partial u_r'}{\partial z}\right)^2} + 3\overline{\left(\frac{\partial u_z'}{\partial r}\right)^2} + 2\overline{\left(\frac{\partial u_r'}{\partial z}\frac{\partial u_z'}{\partial r}\right)}\right\} \quad (6)$$

The volumetric averaged dissipation rates at different Reynolds number using the above-mentioned method are then estimated by

$$\langle \varepsilon \rangle = \frac{1}{\pi(R_o^2 - R_i^2)H} \int_0^H dz \int_{R_i}^{R_o} \nu \left\{ 2\overline{\left(\frac{\partial u_r'}{\partial r}\right)^2} + 2\overline{\left(\frac{\partial u_z'}{\partial z}\right)^2} + 3\overline{\left(\frac{\partial u_r'}{\partial z}\right)^2} + 3\overline{\left(\frac{\partial u_z'}{\partial r}\right)^2} + 2\overline{\left(\frac{\partial u_r'}{\partial z}\frac{\partial u_z'}{\partial r}\right)} \right\} 2\pi r dr \quad (7)$$

The calculated TKE dissipation rate <ε> according to equation (7) is compared with the one obtained by using the empirical correlation (8) shown below as proposed by Wendt *et al*.'s (1933) for estimation of the dimensionless torque in the TCF reactor:

$$G = \begin{cases} 1.45 \frac{\eta^{3/2}}{(1-\eta)^{7/4}} Re^{1.5} & 4 \times 10^2 < Re < 10^4 \\ 0.23 \frac{\eta^{3/2}}{(1-\eta)^{7/4}} Re^{1.7} & 10^4 < Re < 10^5 \end{cases} \quad (8)$$

It can be seen from Figure 11 that the PIV estimated TKE dissipation rates are in general consistent with the empirical correlation estimation results but some deviations are still to exist. At low Reynolds number, lower than around 1.8×10^4, the experimentally measured total dissipation rates are smaller than the results using the empirical correlation prediction. This difference may likely be caused by the measurement error. As the strong reflection at the edge of inner cylinder and outer cylinder, the PIV CCD camera cannot effectively capture the valid visual data in the regions very close to the edges and the cut off from the final image while these regions correspond to where high turbulent energy dissipation rates are generated. For the cases of high Reynolds number, the experimental results are found to be greater than the empirical correlation prediction, this may be attributed to the effect of the background noise on the PIV images.

As the turbulence dissipation rate estimation very much depends on the PIV system's spatial resolution as dissipation is largely contributed by smaller turbulent eddies such as eddies under the Kolmogorov scale. However, those contributions cannot be captured in the PIV system especially in high Re cases. Therefore, to overcome this problem, the use of analogy with Large Eddy Simulation (LES) approach (Sheng *et al*., 2000; Sharp and Adrian, 2001; and Gabriele *et al*., 2009) was employed to estimate the dissipation rate. The filtering method used in the LES is similar to the way to use PIV to obtain the experimental data. Thus, one can also estimate the turbulent energy dissipation rate for those eddies with smaller length scales smaller than PIV using the following equation:

$$\varepsilon_{sgs} = \frac{1}{2}\nu_T\overline{\left(\frac{\partial u_i'}{\partial x_j}+\frac{\partial u_j'}{\partial x_i}\right)^2} = (C_s\Delta)^2 \left\{2\overline{\left(\frac{\partial u_r'}{\partial r}\right)^2}+2\overline{\left(\frac{\partial u_z'}{\partial z}\right)^2}+2\overline{\left(\frac{\partial u_\theta'}{r\partial\theta}\right)^2}+\overline{\left(\frac{\partial u_r'}{\partial z}\right)^2} + \overline{\left(\frac{\partial u_z'}{\partial r}\right)^2}+\overline{\left(\frac{\partial u_r'}{r\partial\theta}\right)^2}+\overline{\left(\frac{\partial u_\theta'}{\partial r}\right)^2}+\overline{\left(\frac{\partial u_z'}{r\partial\theta}\right)^2} + \overline{\left(\frac{\partial u_\theta'}{\partial z}\right)^2}+2\overline{\left(\frac{\partial u_r'}{\partial z}\frac{\partial u_z'}{\partial r}\right)}+2\overline{\left(\frac{\partial u_r'}{r\partial\theta}\frac{\partial u_\theta'}{\partial r}\right)}+2\overline{\left(\frac{\partial u_z'}{r\partial\theta}\frac{\partial u_\theta'}{\partial z}\right)}\right\}^{3/2} \quad (9)$$

$$\nu_T = (C_s\Delta)^2\left[2\overline{\left(\frac{\partial u_r'}{\partial r}\right)^2}+2\overline{\left(\frac{\partial u_z'}{\partial z}\right)^2}+2\overline{\left(\frac{\partial u_\theta'}{r\partial\theta}\right)^2}+\overline{\left(\frac{\partial u_r'}{\partial z}\right)^2}+\overline{\left(\frac{\partial u_z'}{\partial r}\right)^2}+\overline{\left(\frac{\partial u_r'}{r\partial\theta}\right)^2}+\overline{\left(\frac{\partial u_\theta'}{\partial r}\right)^2}+\overline{\left(\frac{\partial u_z'}{r\partial\theta}\right)^2}+\overline{\left(\frac{\partial u_\theta'}{\partial z}\right)^2}+2\overline{\left(\frac{\partial u_r'}{\partial z}\frac{\partial u_z'}{\partial r}\right)}+2\overline{\left(\frac{\partial u_r'}{r\partial\theta}\frac{\partial u_\theta'}{\partial r}\right)}+2\overline{\left(\frac{\partial u_z'}{r\partial\theta}\frac{\partial u_\theta'}{\partial z}\right)}\right]^{1/2} \quad (10)$$

The turbulent eddy viscosity ν_t in the above equation is computed from the grid scale Δ determined from the experiment as the resolution of PIV spatial resolution and Smagorinsky constant *Cs*. A value of Cs = 0.17 has been used following the work of Sheng *et al*. (2000).

In Figure 12, the time-averaged dissipation rate is normalized by spatial- and time-averaged dissipation rate in each Re condition. From the figure, it indicates that the distribution of TKE dissipation rate reveals that high turbulent energy dissipation rate in the Taylor Couette flow reactor mainly takes place in the jet flow part and counter-flowing region, while the one in the jet flow area is higher than the one in the counter-flowing region. In low Re case, Re_T = 7300, the boundary between high and low TKE dissipation rate region is clear. Smaller $\bar{\varepsilon}$ dominates a large area of Taylor vortex cores. As Re_T increases, the boundary starts to become vague and the area of $\bar{\varepsilon}/\langle\bar{\varepsilon}\rangle = 1$ gradually spreads. This can be clearly seen from Figure 12, where probability density of $\bar{\varepsilon}/\langle\bar{\varepsilon}\rangle$ for different Re_T number is presented. In case of low Reynolds number, there is only one peak of the probability density (or with two very small closed peaks) to occur as can be observed from the figure, indicating the low $\bar{\varepsilon}$ to occupy the most regions of the vortices. However, as Re_T increases, two peaks are observed from the probability density distribution as shown in the figure. Eventually, two peaks can be clearly observed in Figure 12 in case of high Reynolds number. The second peak with the value around $\bar{\varepsilon}/\langle\bar{\varepsilon}\rangle = 1$ shows the fact that more areas of the vortices with the averaged TKE dissipation rate can be observed for the cases of high Reynolds number. This indicates that with increase in Re_T, the TCR system

changes from a relatively low TKE dissipation rate dominated system with limited high dissipation rate areas to an averaged TKE dissipation rate dominated system, i.e. the flow pattern becomes fully turbulent. Therefore, this phenomenon can be used to control small scale process such as micro-mixing process.

3.4 Characteristics of shear turbulence using TKE power spectrum and spatial correlation

In order to clearly indicate the characteristics of shear turbulence in the TC reactor, the TKE spectra at different radial positions, $(r\text{-}R_i)/(R_o\text{-}R_i)$ = 0.02, 0.50 and 0.98, are calculated using the PIV measurement data, corresponding to the spectrum attained in the vicinity of rotating inner cylinder, in the bulk and near the region of the wall of outer cylinder.

$$\overline{E_{zz}}(r,\lambda) = \frac{1}{T}\int_0^T \left(\frac{2}{\pi}\int_0^\infty \overline{u'(r,z_0)u'(r,z_0+\Delta z)}cos(\lambda z)dz\right)dt \tag{11}$$

Such correlation spectrum for cases of different Reynolds number are shown in Figure 14, where the power spectrum was obtained by time averaging of the spatially averaged turbulent kinetic energy spectrum at different positions along the TC reactor height at three given radial locations as mentioned. The purpose of taking such advantage is to better characterise the impact of the Taylor vortex structures on induced shear turbulence. From Figure 14, in most conditions, the TKE contained in larger length scale for Erz is smaller than that of Ezz, indicating that the TKE of eddies in the large scale is strongly affected by the boundary geometry (in the present investigation case, the space in the axial direction is 10 times of that in the radial direction, i.e. $\Gamma = H/d = 10$). For both the spectrums in radial positions of $(r\text{-}R_i)/(R_o\text{-}R_i)$ = 0.02 and 0.98, the TKE corresponding to the largest length scale of eddies shown in E_{zz} is roughly 10 times of that of E_{rz}, which seems to follow the aspect ratio of $\Gamma = 10$. However, for case of $(r\text{-}R_i)/(R_o\text{-}R_i)$ = 0.50, the TKE of the largest length scale of eddies shown for E_{zz} is almost the same as that of E_{rz}. This indicates that in the core regions of the TC reactor, the TKE may be likely less affected by the boundary conditions. Another phenomenon that needs to be pointed out is that for most of the conditions, the slope of the TKE spectrum tends to vary from -5/3 to a relatively steeper value close to -3. This indicates that at relatively lower Reynolds number (7300 in this case), the flow pattern is in TTCF regime but the flow exhibits stronger non-isotropic behaviour, especially near the inner cylinder wall. However, as Reynolds number increases, the flow pattern may evolve and enter FTF regime (Re > 20000) where isotropy of

the turbulence starts to improve as the slope becomes less steep. It can be also seen from Figure 14 that the TKE in the wave number range of 20-1000 in the vertical direction is greater than that in the radial direction near both walls. This may indicate that due to the inner wall rotation, less fluctuation energy in the vertical direction is generated than the wall surface in circumferential direction. This may need further investigation.

Spatial correlation coefficient $\frac{\overline{u'(r,z_0)u'(r,z_0+z)}}{\overline{u'^2(r,z_0)}}$ of time averaged TKE along the TCF reactor at different radial locations is shown in Figure 15. From this figure, the correlation coefficient fluctuates in regular pattern but gradually reduces along the height indicates that the Taylor vortex structures have undergone deformation. In fact, this can be affirmed by the aspect ratio of Taylor vortices as can be seen from Figure 3.

4. Conclusions

In this study, PIV technology was adopted to investigate shear turbulence characteristics based on the measurement of the $r-\theta$ plane of the annulus between the rotating inner and non-rotating outer cylinder in a large size TCF reactor. The experimental results indicated that when Reynolds number $Re_T = \frac{r_i \omega d_{gap}}{\nu}$ is greater than 7300, the vorticity of Taylor vortices remarkably increases, consequently causing the outflow between the pair of Taylor vortices to form a much stronger outward impinging jet. The following points can be concluded from this study:

(1) Taylor vortices patterns can be still well recognized based on the time-averaged flow fields for the Reynolds number Re_T varying from 1800 to 21600. The typical Taylor vortex structures start to disappear when the Reynolds number further increases and is greater than 21600.

(2) From both vorticity and dissipation rate probability density distribution, the two peaks distribution nature of TCF are revealed. The secondary vortices formed between a pair of Taylor vortices in the vicinity of the outer cylinder's inner surface are observed and the patterns look quite regular. Such secondary vortices have a major effect on the outward impinging jet flow formed in the gap of TCF vortex cells.

(3) The centrifugal force has a larger influence in low Re case than high Re case relatively as the amplitude of dimensionless radical velocity decreases with Reynolds number. It was demonstrated that, especially in radical and axial direction, gravity force, because of the experimental rig is vertical placed, influences the flow in direction but such effect in its parallel direction is much stronger than that in normal direction.

(4) Turbulent energy dissipation rate distribution was obtained using 2D PIV measured turbulent velocity fluctuation gradients. By using the analogy with the large eddy simulation for calculation of the sub-grid dissipation rate, the volume-averaged TKE dissipation rate calculated based on the PIV measurements are found to be well agreed with the estimation value but using the empirical relation as suggested by Wendt *et al*. (1933).

(5) Spatial correlation coefficient $\frac{\overline{u'(r,z_0)u'(r,z_0+z)}}{\overline{u'^2(r,z_0)}}$ of time averaged TKE k along the TCF reactor at different radial locations can be used to characterize the shear turbulence in the TCF reactor. The spatial correlation coefficient fluctuates in regular pattern but gradually reduces along the height, indicating the Taylor vortex structures to have undergone deformation.

Acknowledgements

The authors would like to thank the National Natural Science Foundation of China for financial support (Grant Nos. 21576141, 21761132026). This work is also supported by the scholarship of International Doctoral Innovation Centre (IDIC) of the University of Nottingham Ningbo China and EPSRC (Grant no. EP/G037345/1).

References

Akonur, A., & Lueptow, R. M. (2003). Three-dimensional velocity field for wavy Taylor–Couette flow. *Physics of Fluids*, 15(4), 947-960.

Andereck, C. D., Liu, S. S., & Swinney, H. L. (1986). Flow regimes in a circular Couette system with independently rotating cylinders. *Journal of fluid mechanics*, 164, 155-183.

Coles, D. (1965). Transition in circular Couette flow. *Journal of Fluid Mechanics*, 21(3), 385-425.

Deng, R., Arifin, D. Y., Mak, Y. C., & Wang, C. H. (2009). Characterization of Taylor vortex flow in a short liquid column. *AIChE journal*, 55(12), 3056-3065.

Dusting, J., & Balabani, S. (2009). Mixing in a Taylor–Couette reactor in the non-wavy flow regime. *Chemical engineering science*, 64(13), 3103-3111.

Gabriele, A., Nienow, A. W., & Simmons, M. J. H. (2009). Use of angle resolved PIV to estimate local specific energy dissipation rates for up-and down-pumping pitched blade agitators in a stirred tank. *Chemical Engineering Science*, 64(1), 126-143.

Gorman, M., & Swinney, H. L. (1979). Visual observation of the second characteristic mode in a quasiperiodic flow. *Physical Review Letters*, 43(25), 1871.

Haut, B., Amor, H. B., Coulon, L., Jacquet, A., & Halloin, V. (2003). Hydrodynamics and mass transfer in a Couette–Taylor bioreactor for the culture of animal cells. *Chemical Engineering Science*, 58(3-6), 777-784.

Huisman, S. G., van Gils, D. P., Grossmann, S., Sun, C., & Lohse, D. (2012). Ultimate turbulent taylor-couette flow. *Physical review letters*, 108(2), 024501.

Hunt, JCR., Wray, A., & Moin, P. (1988). Eddies, stream, and convergence zones in turbulent flows. *Centre for turbulence research report* CTR-S88, 193-208.

Judat, B., Racina, A., & Kind, M. (2004). Macro-and micromixing in a Taylor-Couette reactor with axial flow and their influence on the precipitation of barium sulfate. *Chemical Engineering & Technology: Industrial Chemistry-Plant Equipment-Process Engineering-Biotechnology*, 27(3), 287-292.

Lee, S. H., Chung, H. T., Park, C. W., & Kim, H. B. (2009). Experimental investigation of the effect of axial wall slits on Taylor–Couette flow. *Fluid dynamics research*, 41(4), 045502.

Liu, D., Kang, I. S., Cha, J. E., & Kim, H. B. (2011). Experimental study on radial temperature gradient effect of a Taylor–Couette flow with axial wall slits. *Experimental thermal and fluid science*, 35(7), 1282-1292.

Mao, Y., Chang, Q., Zeng, L., & Yu, C. (2013). Velocity field structure and flocculation efficiency in Taylor-Couette flow. *Separation Science and Technology*, 48(4), 659-663.

Qiao, J., Deng, R., & Wang, C. H. (2015). Particle motion in a Taylor vortex. *International Journal of Multiphase Flow*, 77, 120-130.

Racina, A., & Kind, M. (2006). Specific power input and local micromixing times in turbulent Taylor–Couette flow. *Experiments in fluids*, 41(3), 513-522.

Randolph, A. D. and Larson, M. A. (1988). Theory of Particulate Processes, 2nd edition. *Academic Press*, New York, U.S.A

Ravelet, F., Delfos, R., & Westerweel, J. (2010). Influence of global rotation and Reynolds number on the large-scale features of a turbulent Taylor–Couette flow. *Physics of Fluids*, 22(5), 055103.

Sharp, K. V., & Adrian, R. J. (2001). PIV study of small-scale flow structure around a Rushton turbine. *AIChE Journal*, 47(4), 766-778.

Sharp, K. V., Kim, K. C., & Adrian, R. (2000). Dissipation estimation around a Rushton turbine using particle image velocimetry. In Laser Techniques *Applied to Fluid Mechanics* (pp. 337-354). Springer, Berlin, Heidelberg.

Sheng, J., Meng, H., & Fox, R. O. (2000). A large eddy PIV method for turbulence dissipation rate estimation. Chemical engineering science, 55(20), 4423-4434.

Smieszek, M., & Egbers, C. (2005). Flow structures and stability in Newtonian and non-Newtonian Taylor-Couette flow. In Journal of Physics: Conference Series (Vol. 14, No. 1, p. 010). IOP Publishing.

Smith, G. P., & Townsend, A. A. (1982). Turbulent Couette flow between concentric cylinders at large Taylor numbers. *Journal of Fluid Mechanics*, 123, 187-217.

Takeda, Y. (1999). Quasi-periodic state and transition to turbulence in a rotating Couette system. *Journal of Fluid Mechanics*, 389(1), 81-99.

Taylor, G. I. (1923). VIII. Stability of a viscous liquid contained between two rotating cylinders. *Philosophical Transactions of the Royal Society of London. Series A, Containing Papers of a Mathematical or Physical Character*, 223(605-615), 289-343.

Tokgoz, S., Elsinga, G. E., Delfos, R., & Westerweel, J. (2012). Spatial resolution and dissipation rate estimation in Taylor-Couette flow for tomographic PIV. *Experiments in fluids*, 53(3), 561-583.

Tong, P., Goldburg, W. I., Huang, J. S., & Witten, T. A. (1990). Anisotropy in turbulent drag reduction. *Physical review letters*, 65(22), 2780.

Wang, L., Olsen, M. G., & Vigil, R. D. (2005). Reappearance of azimuthal waves in turbulent Taylor–Couette flow at large aspect ratio. *Chemical engineering science*, 60(20), 5555-5568.

Watanabe, K., Takayama, T., Ogata, S., & Isozaki, S. (2003). Flow between two coaxial rotating cylinders with a highly water-repellent wall. *AIChE journal*, 49(8), 1956-1963.

Wendt, F., (1933). Turbulente Stromungen Zwishen Zwei Rotierender Konaxialen Zylindem. *Ingenieur-Archiv*, Vol. IV, p. 577.

Wereley, S. T., & Lueptow, R. M. (1998). Spatio-temporal character of non-wavy and wavy Taylor–Couette flow. *Journal of Fluid Mechanics*, 364, 59-80.

Wereley, S. T., & Lueptow, R. M. (1999). Velocity field for Taylor–Couette flow with an axial flow. *Physics of Fluids*, 11(12), 3637-3649.

Table 1: Examples of previous studies on Taylor-Couette flows using the PIV technology

Authors	Year	TC Configuration (R_i×R_o×H in mm)	PIV	Operation Re
Qiao, Deng, & Wang	2015	20×30×60	2D	<150
Wereley & Lueptow	1998	43.4×52.3×424.53	2D	<202
Wereley & Lueptow	1999	43.4×52.3×414.74	2D	<215
Smieszek & Egbers	2005	N/A	2D	<259
Dusting & Balabani	2009	20.6×25.5×54.88	2D	<330
Akonur & Lueptow	2003	42.4×52.1×463.66	3D	<488
Deng, Arifin, Mak, & Wang	2009	18.4×30×200	2D	<519
Judat, Racina, & Kind	2004	68×100×200	2D	<705
Watanabe, Takayama, Ogata, & Isozaki	2003	81×120×240	2D	<900
Liu, Kang, Cha, & Kim	2011	33×40×336	2D	<1050
Haut, Amor, Coulon, Jacquet, & Halloin	2003	40×48.5×90	2D	<1600
Lee, Chung, Park, & Kim	2009	33×40×336	2D	<2863
Wang, Olsen, & Vigil,	2005	34.925×47.625×431.8	2D	<5500
Ravelet, Delfos, & Westerweel	2010	110×120×220	2D	<10000
Mao, Chang, Zeng, & Yu	2013	37.5×50×440	2D	<20000
Tokgoz, Elsinga, Delfos, & Westerweel	2012	110×120×220	3D	<23500
Racina & Kind	2006	100×113×390	2D	<25000
Huisman, van Gils, Grossmann, Sun, & Lohse	2011	200×279×927	2D	<110730

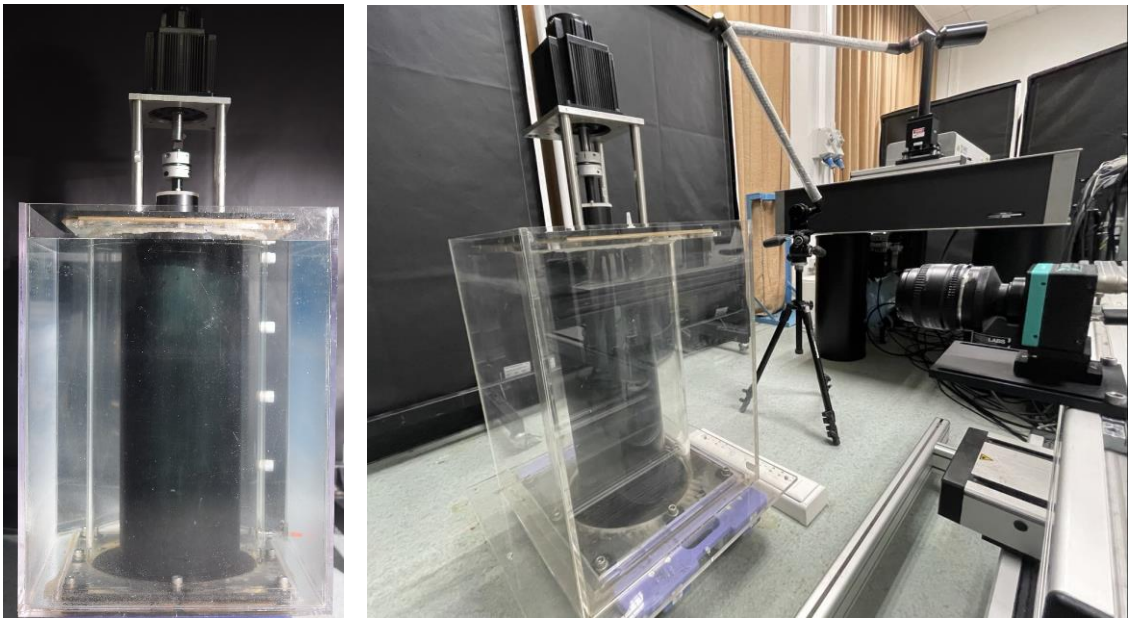

(a) (b)

Figure 1. (a) Experimental rig with working fluid half full to indicate the gap, (b) DANTEC Dynamics 2D-PIV system.

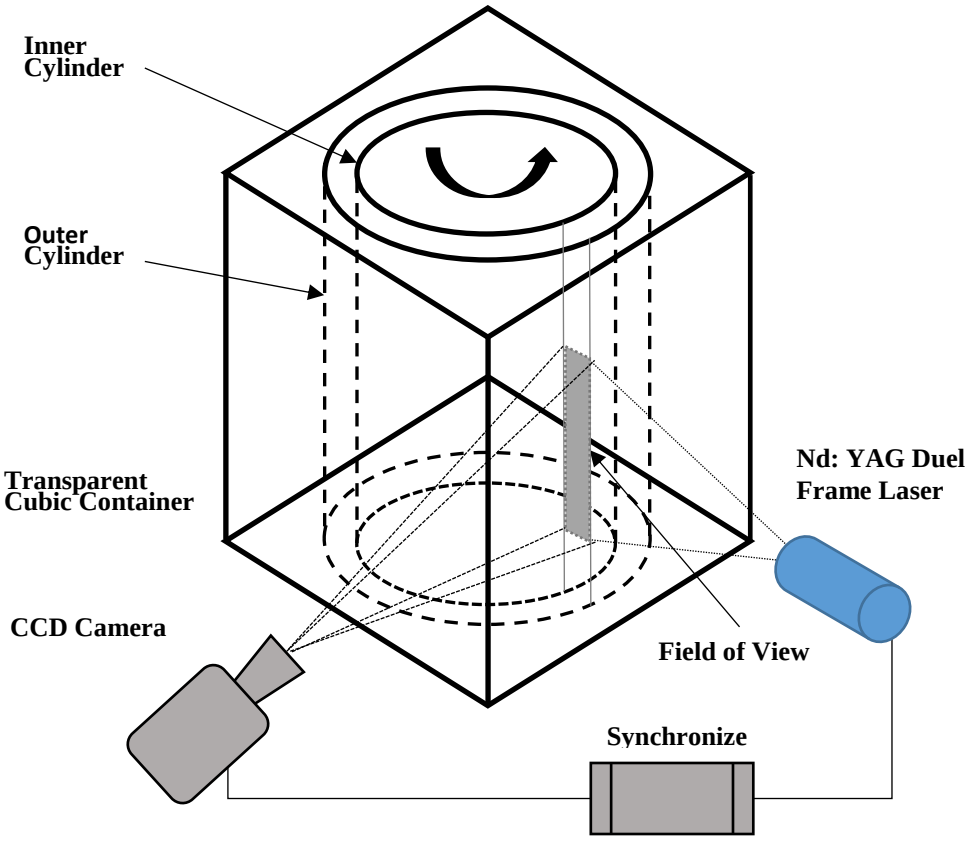

Figure 2. Schematic illustration of the PIV experimental setup for measurement of a large size Taylor-Couette flow reactor.

(a) (b) (c) (d)

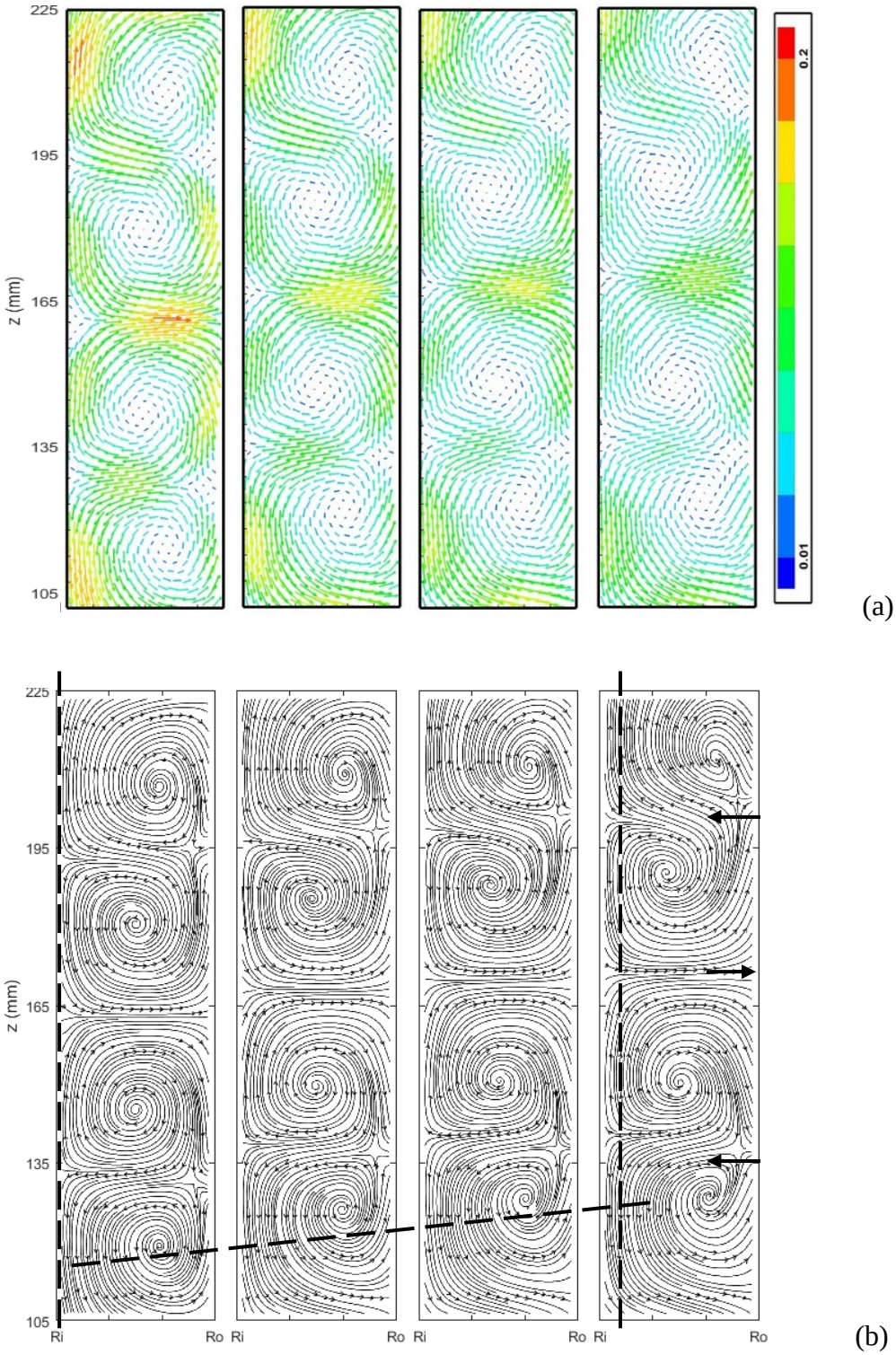

Figure 3. (a) Time averaged velocity field; and (b) Time averaged streamlines taken in the measured section of Taylor-Couette flow reactor at different Reynolds number. The velocity vector has been colour normalized by the maximum velocity for the corresponding Reynolds number case.

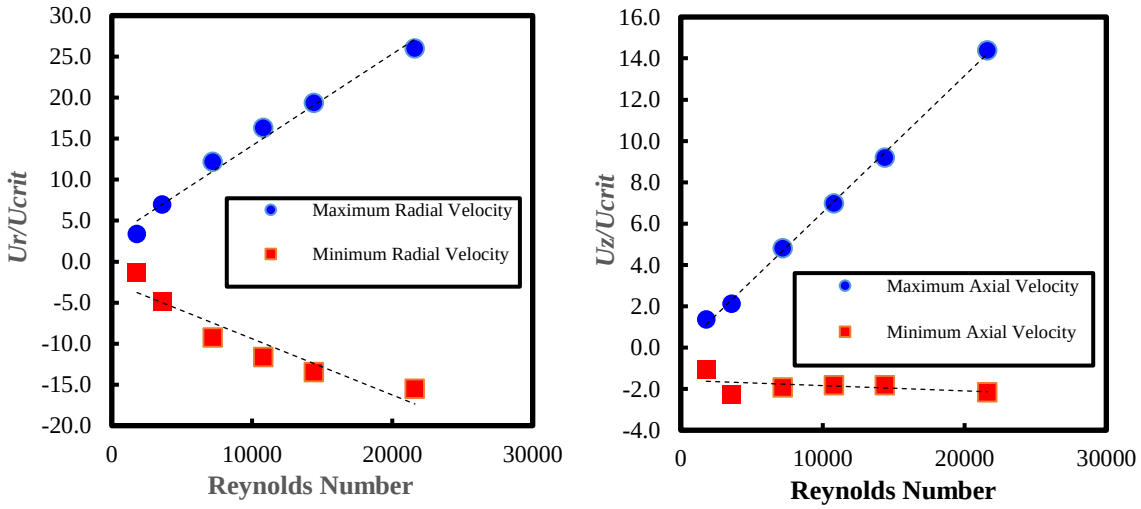

(a) (b)

Figure 4. Maximum and minimum averaged velocity in the vertical centrelines normalized by inner cylinder edge velocity at critical Reynolds number variation with increasing Reynolds number: (a) radial velocity, (b) axial velocity.

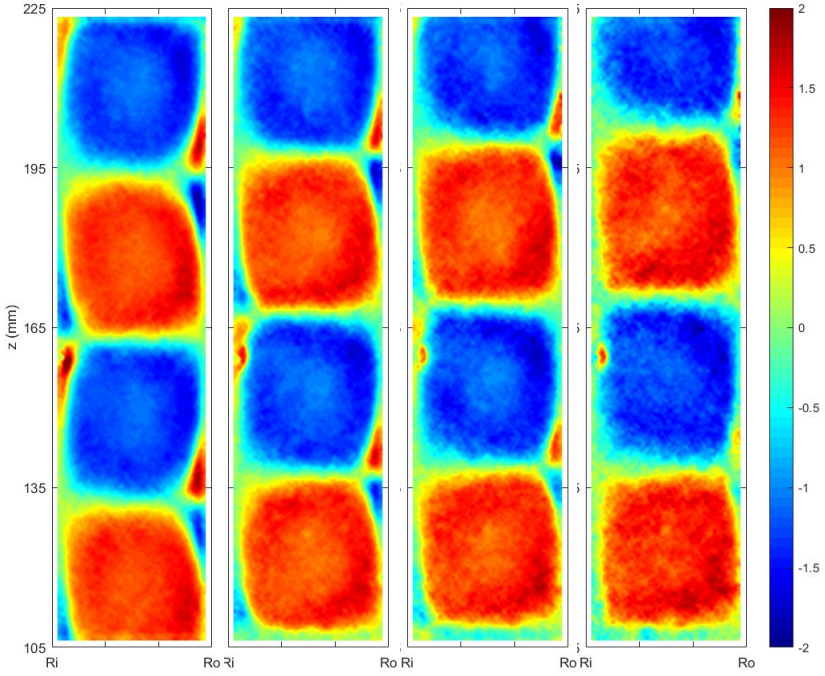

(a) (b) (c) (d)

Figure 5. Time averaged $\bar{\omega}/\langle\bar{\omega}\rangle$ contour of different Reynolds number: (a) Re=7300, (b) Re=11500, (c) Re=15000, (d) Re=21300.

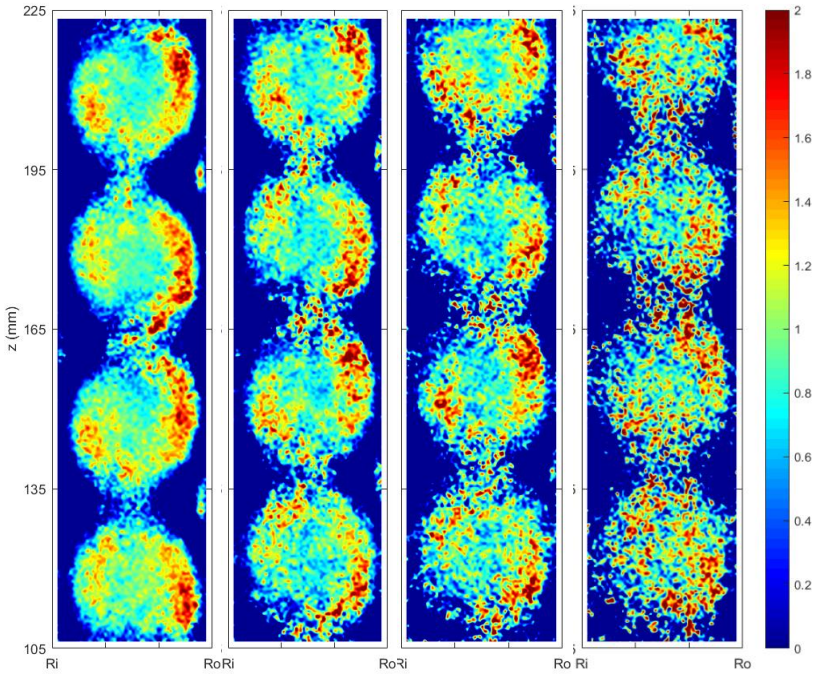

(a) (b) (c) (d)

Figure 6. Time averaged $\overline{Q}/\langle\overline{Q}\rangle$ contour of different Reynolds number: (a) Re=7300, (b) Re=11500, (c) Re=15000, (d) Re=21300.

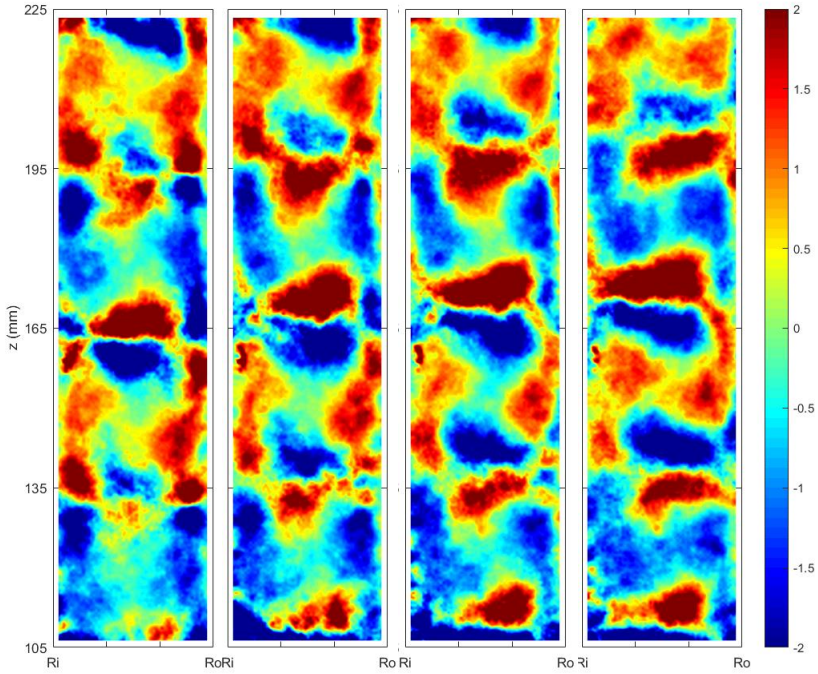

(a) (b) (c) (d)

Figure 7. Time-averaged $\overline{\tau_{rz}}/\langle\overline{\tau_{rz}}\rangle$ contour of different Reynolds number: (a) Re=7300, (b) Re=11500, (c) Re=15000, (d) Re=21300.

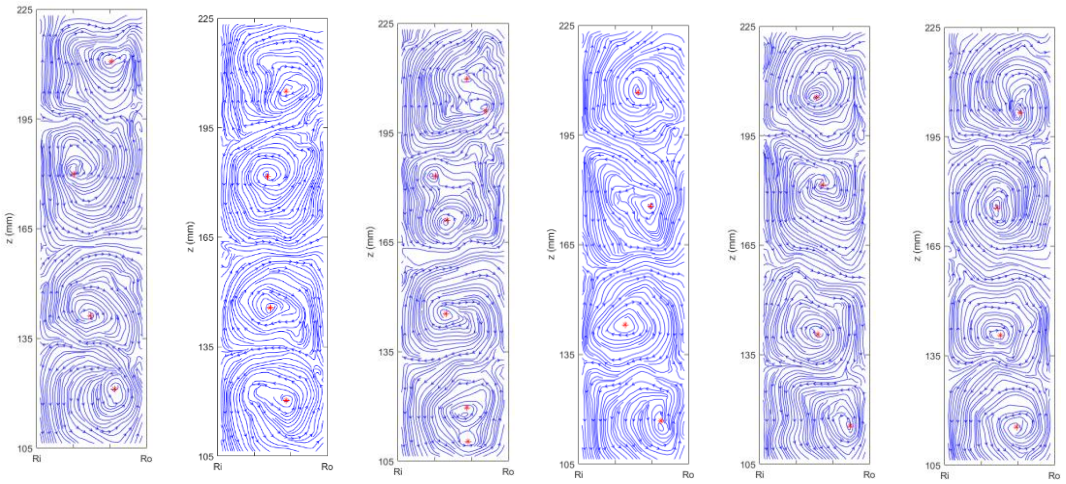
225
195
165
135
105
z (mm)
Ri
Ro

(a)

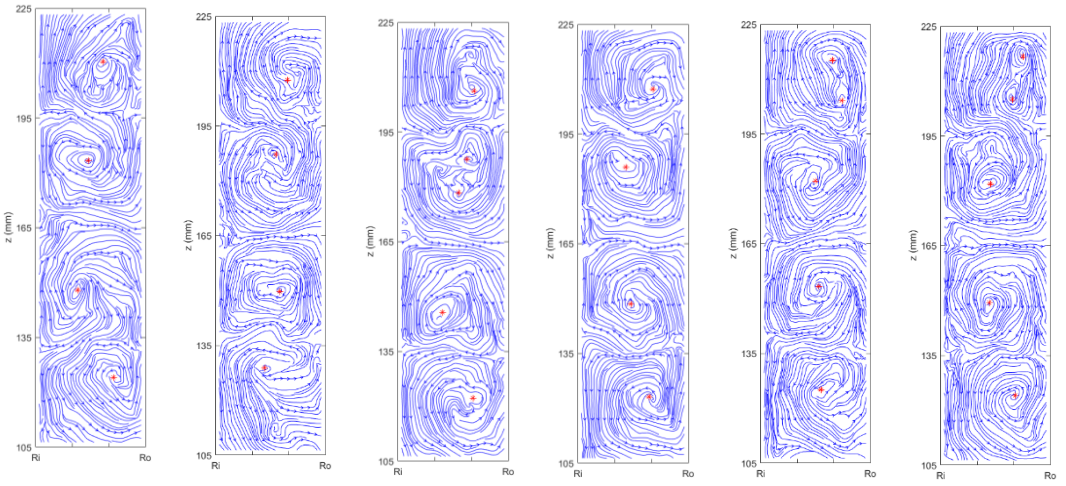
225
195
165
135
105
z (mm)
Ri
Ro

(b)

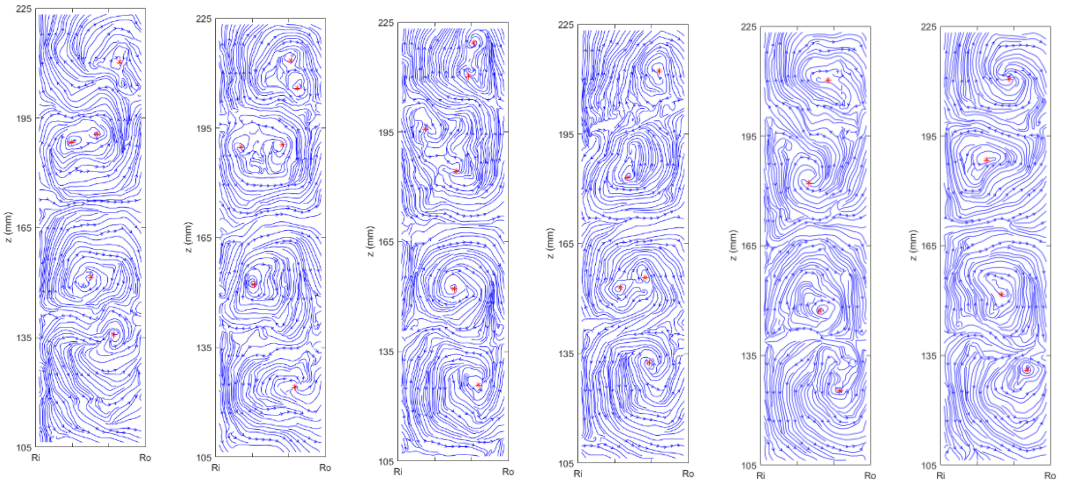
225
195
165
135
105
z (mm)
Ri
Ro

(c)

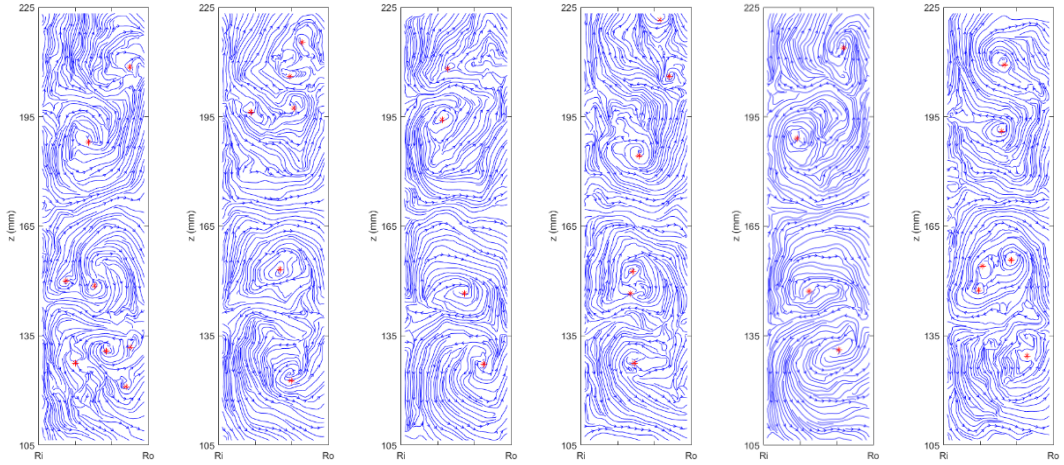

(d)

Figure 8. Instantaneous streamline sequence of different Reynolds number: (a) Re=7300, (b) Re=11500, (c) Re=15000, (d) Re=21300.

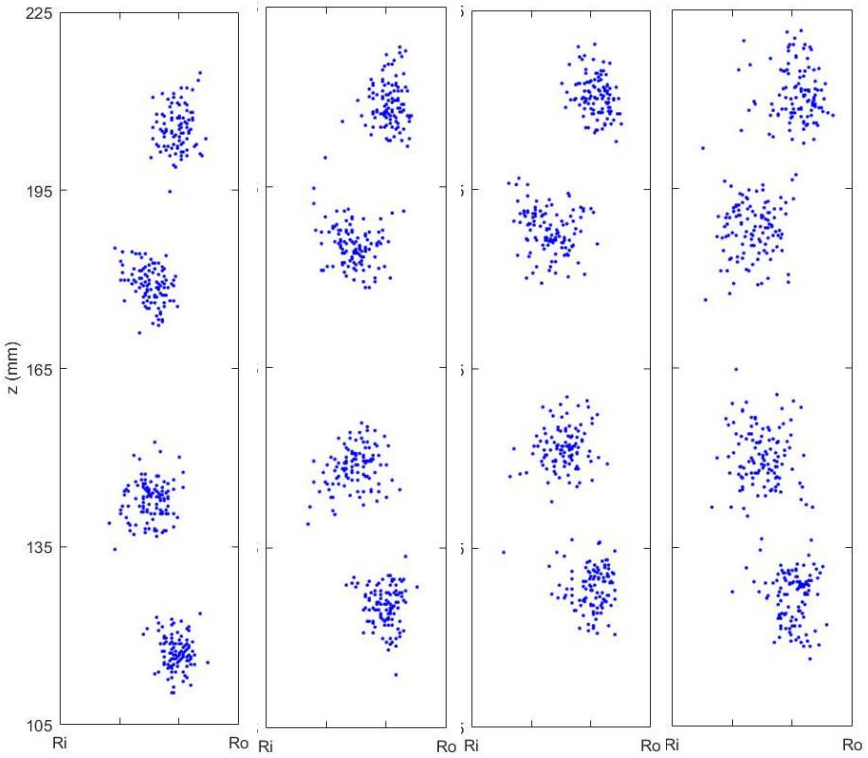

(a) (b) (c) (d)

Figure 9. The core position variations of Taylor vortices at different Reynolds number: (a) Re=7300, (b) Re=11500, (c) Re=15000, (d) Re=21300.

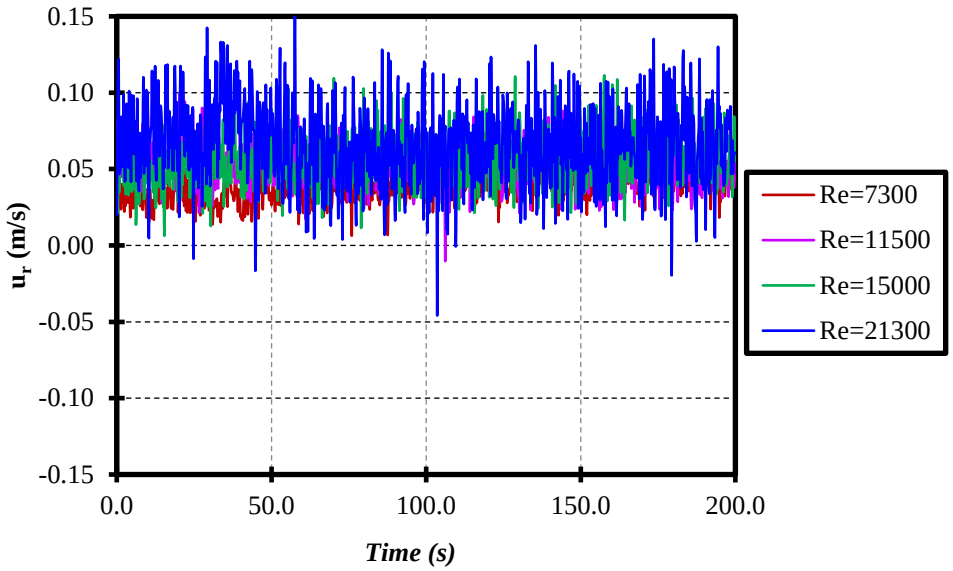

(a)

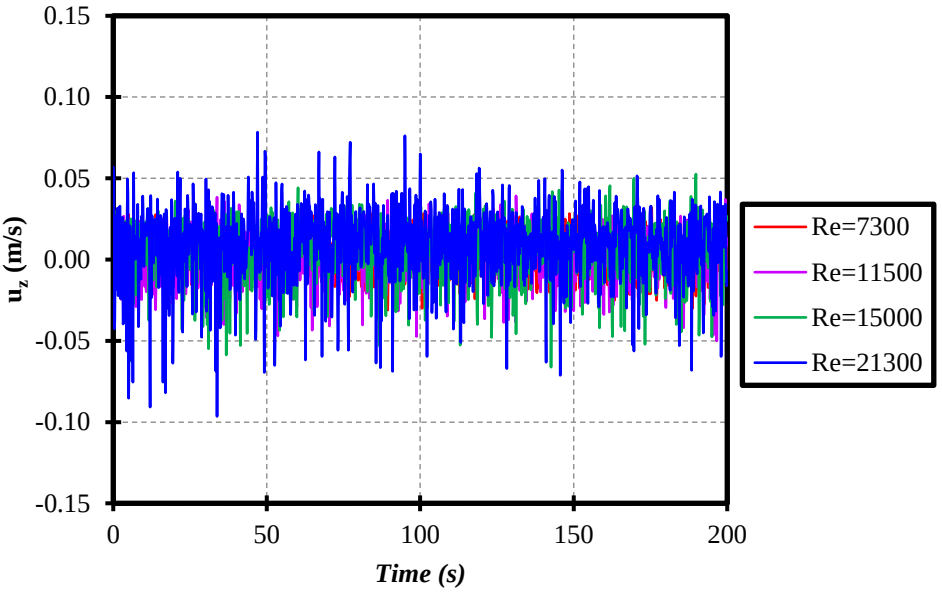

(b)

Figure 10. Instantaneous velocity components of u_r and u_z for a period of 200 s obtained by using 2D PIV at location of $r = \frac{d_{gap}}{2}, z = \frac{H}{2}$.

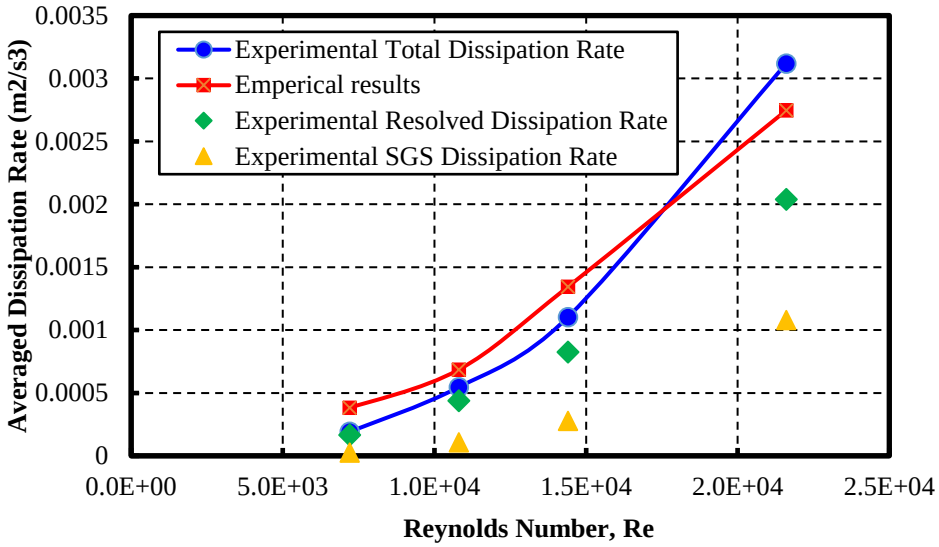

Figure 11. Comparison of TKE dissipation rates obtained from the PIV data and from the estimation by using the empirical relationship proposed by Wendtl *et al* (1933).

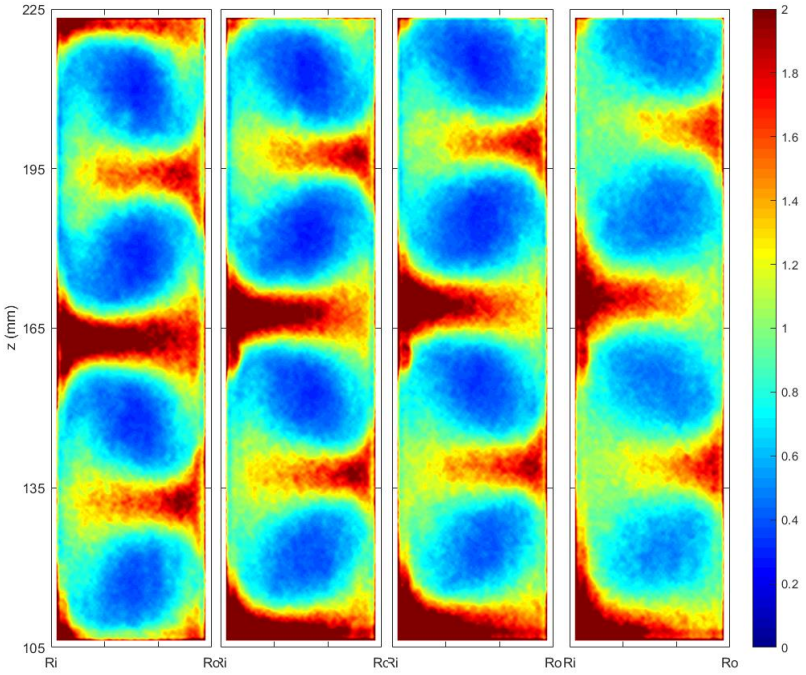

(a) (b) (c) (d)

Figure 12. Non-dimensionless time-averaged turbulence energy dissipation rate $\bar{\varepsilon}/\langle\bar{\varepsilon}\rangle$ at different Reynolds number: (a) Re=7300, (b) Re=11500, (c) Re=15000, (d) Re=21300.

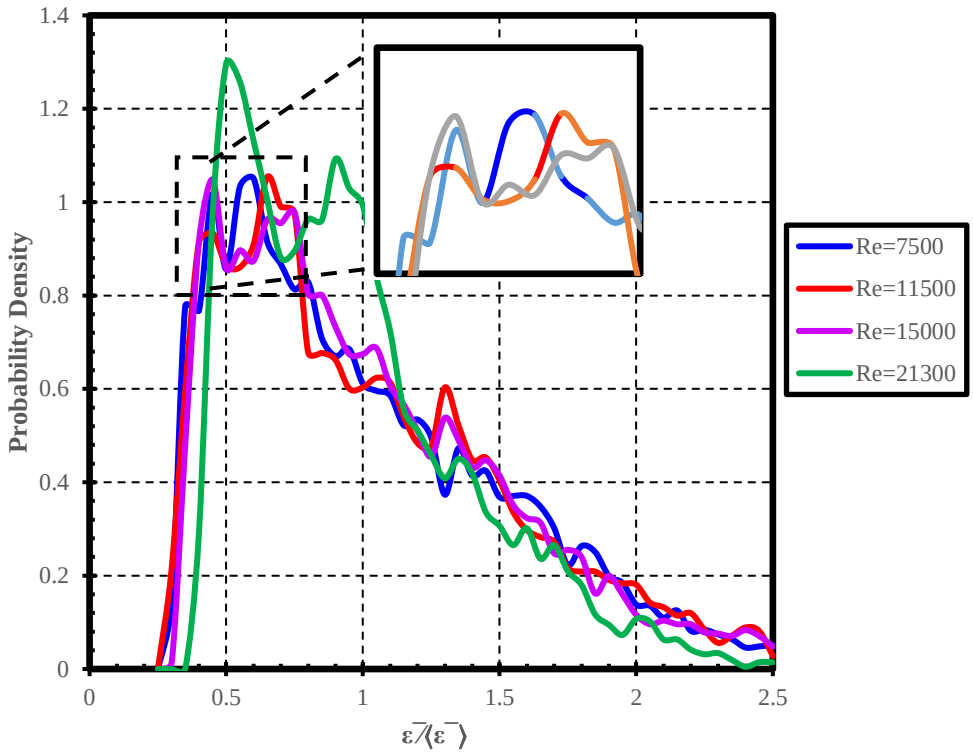

Figure 13. Probability density distribution of time averaged TKE dissipation rate $\bar{\varepsilon}/\langle\bar{\varepsilon}\rangle$ distributed in the measuring plane.

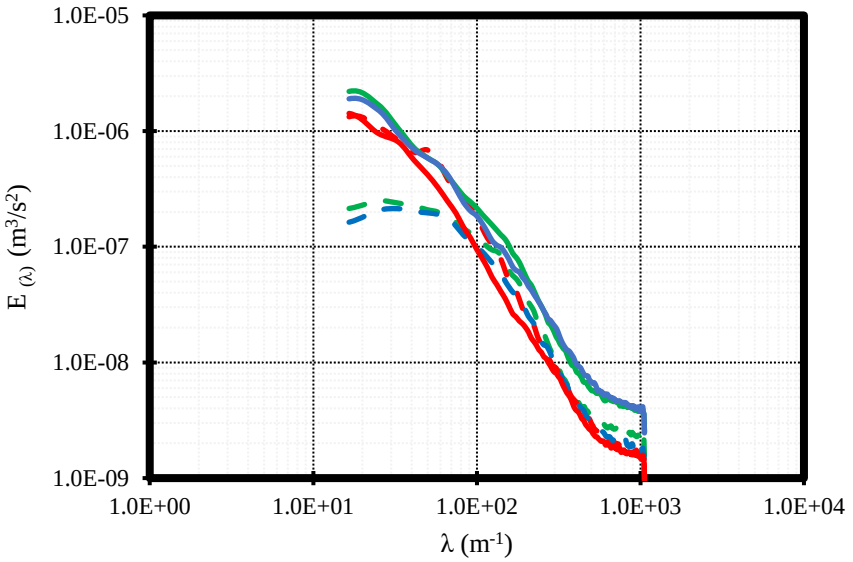
1.0E-05
1.0E-06
1.0E-07
1.0E-08
1.0E-09
E (λ) (m3/s2)
1.0E+00
1.0E+01
1.0E+02
1.0E+03
1.0E+04
λ (m-1)

(a)

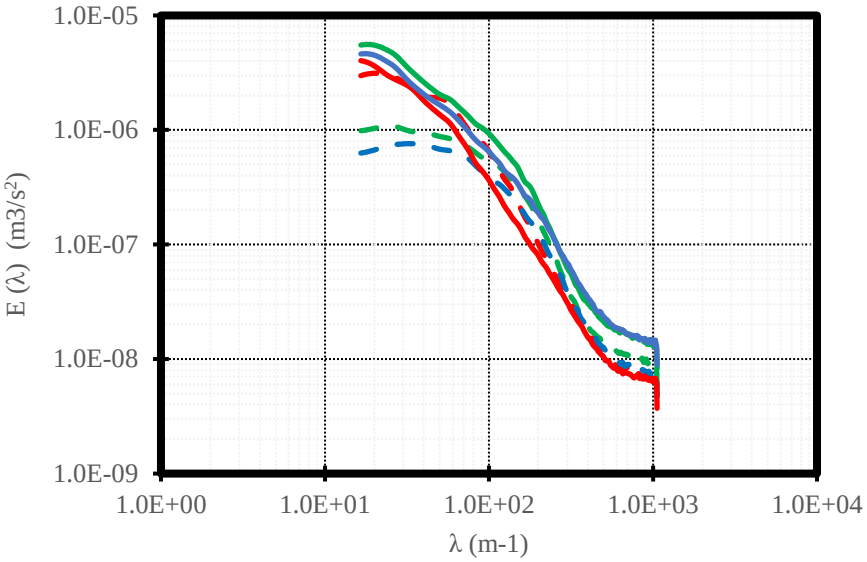
1.0E-05
1.0E-06
1.0E-07
1.0E-08
1.0E-09
E (λ) (m3/s2)
1.0E+00
1.0E+01
1.0E+02
1.0E+03
1.0E+04
λ (m-1)

(b)

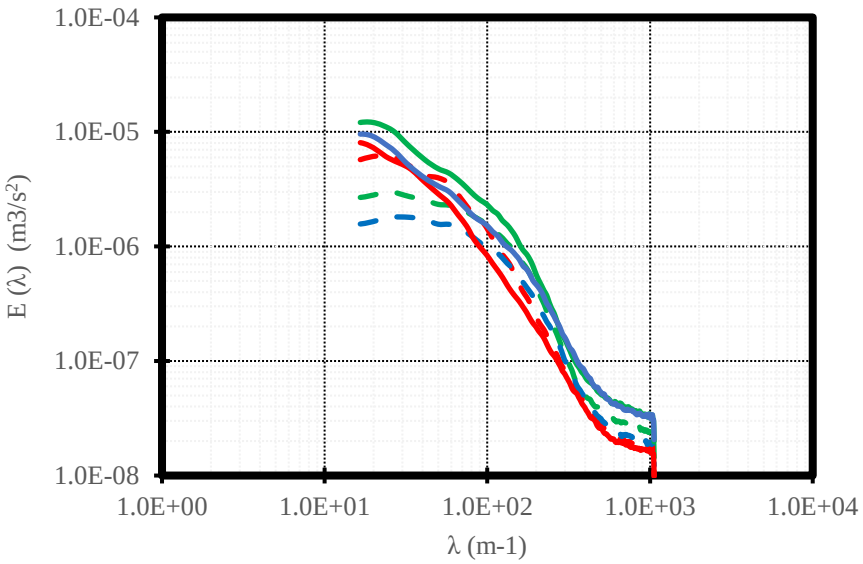

(c)

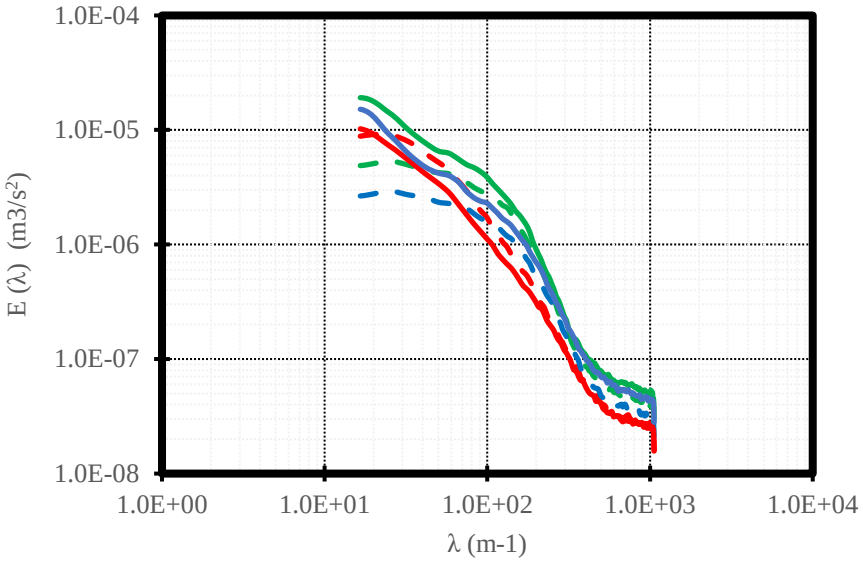

(d)

Figure 14. Energy spectrum from spatial autocorrelation function of different radial position: (a) Re = 7200, (b) Re = 10800, (c) Re = 14400, (d) Re = 21600.

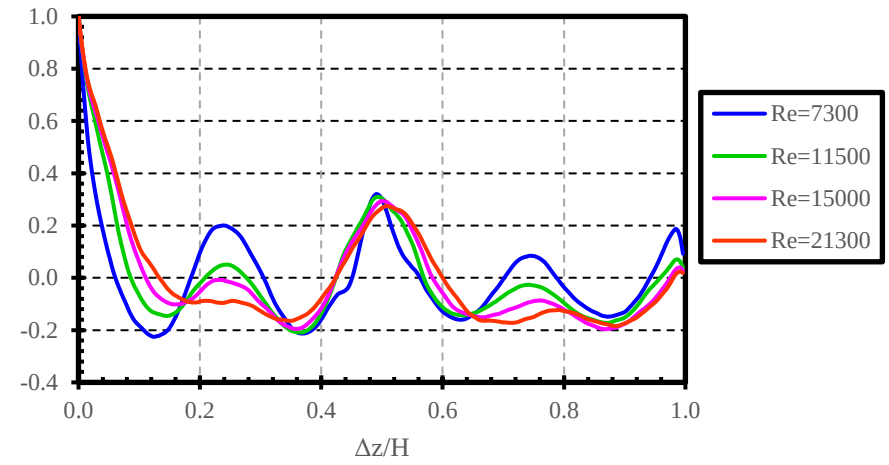

(a)

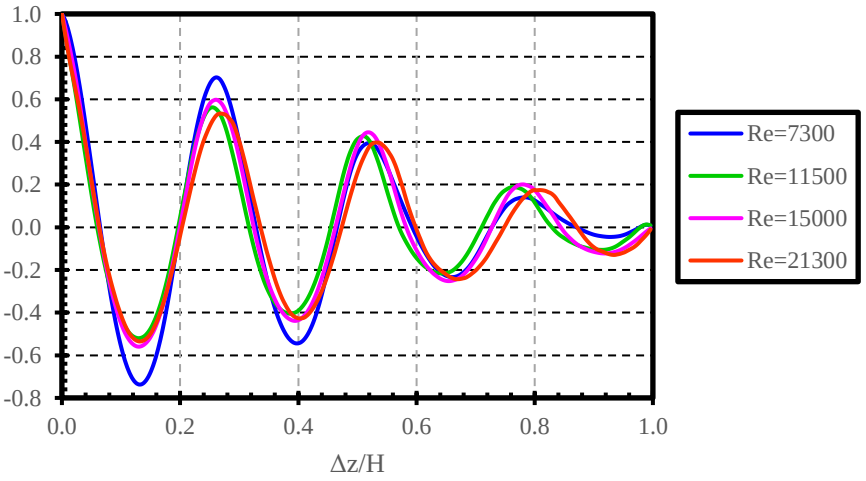

(b)

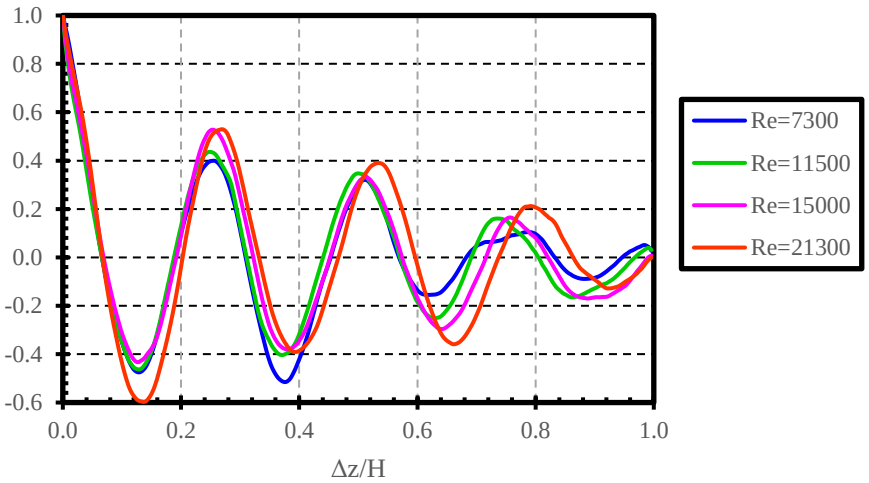

(c)

Figure 15. Spatial correlation $\frac{\overline{k(z_0)k(z_0+z)}}{\overline{k^2(z_0)}}$ of time averaged TKE k along the Taylor-Couette flow reactor at different radial locations(a) $(r\text{-}R_i)/d_{gap}$=0.05, (b) $(r\text{-}R_i)/d_{gap}$=0.5, (c) $(r\text{-}R_i)/d_{gap}$=0.95.